

Flow characteristics of viscoelastic fluids in an abrupt contraction by using numerical modeling

P. Saramito ¹ and J. M. Piau *

Laboratoire de Rhéologie ², B.P. 53, 38041 Grenoble Cedex 9, France

(Received September 26, 1993; in revised form February 7, 1994)

Abstract

Consideration is given to the influence of elongational properties on flow characteristics in the case of shear-thinning highly elastic fluids in an abrupt contraction. Sufficient data has been published to demonstrate that viscoelasticity can have a significant effect on flow characteristics in abrupt contractions. This paper reports on numerical experiments with four representative test-fluids of Phan-Thien–Tanner models. Furthermore, a new dimensionless number that takes into account elongational properties is proposed.

Of major importance is the observation that the vortex enhancement and the energy loss in the entrance region both vary strongly with the elongational properties of Phan-Thien–Tanner models. Numerical results are qualitatively in good agreement with experimental measurements on polymer solutions and melts.

Finally, this numerical study provides a fundamental basis, which may be quite useful for the prediction of viscoelastic fluid flows by using numerical modeling, and for the calculation of rheometrical properties of viscoelastic fluids through constitutive equation parameter adjustment.

Keywords: abrupt contraction; elongational properties; energy losses; numerical modeling; viscoelasticity; vortex enhancement

* Corresponding author.

¹ Present address: Institut National Polytechnique, 46 avenue F. Viallet, 38000 Grenoble, France.

² Université Joseph Fourier Grenoble I, et Institut National Polytechnique de Grenoble, Associé au CNRS (URA 1510).

1. Introduction

One of the difficult problems in viscoelastic fluid mechanics is to analyze the relationship between macroscopic features of complex flows in an abrupt contraction, such as vortex pattern, energy loss, . . . and its viscous behaviour in simple shear and extensional flows.

Understanding entry flow of viscoelastic fluids is of importance in fundamental flow-property measurement and in extrusion of polymer melts and solutions. Furthermore, the characteristics of vortices and flow curves are of particular interest in the design of extrusion dies.

In a number of cases, numerical simulations of complex flows predict a correct qualitative behavior but fail to produce quantitative agreement on the value of the Weissenberg number. In a recent paper, Boger, Crochet and Keiller [1] have proposed a definition of the Weissenberg number in abrupt contraction flow problems. By using the White–Metzner model, that predicts a finite time relaxation parameter for high shear rate, they obtain finite values of the Weissenberg number for high flow rates. Nevertheless, this definition is not completely satisfying: it does not apply successfully to other models, such as the Phan-Thien–Tanner model. Furthermore, it does not take into account the elongational properties of viscoelastic flows in abrupt contractions. However, experimental results show that elongational properties in the entrance region appear as a major factor for the vortex enhancement [2,3]. It was also shown on the basis of numerical simulation that the elongational viscosity leads to an increase of the vortex activity and pressure drop (see [4–7] and related works).

In this paper, four shear thinning fluids in a circular 8 to 1 abrupt contraction are considered. The first fluid presents a monotonically decreasing elongational viscosity versus the elongation rate. The second one develops an elongational viscosity that reaches a maximum and then decays. The third and the fourth have monotonically increasing elongational viscosities that reach plateaus.

The second section presents the Phan-Thien–Tanner models [8,9], which make relatively good predictions for shear and elongational material properties, and allows one to cover expected properties both for polymer solutions and melts for the full range of molecular weight variations. A preselection of models based on simple kinematics like uniaxial elongation and shear flows will be considered. The Weissenberg number defined in [1] and a dimensionless number that takes into account elongational properties of such models will be introduced.

The third section gives an overview of the numerical method: a time-dependent approach and a finite element method [10,11]. This numerical strategy will allow us to obtain in an efficient way stationary solutions for complex flows of viscoelastic fluids.

The fourth section presents numerical results for a circular abrupt 8 to 1 contraction. Flow patterns and vortex activity are exhibited for a large range of flow rates. The computation of the energy loss in the entrance region is also provided. A careful analysis of the flow curves and the Couette correction is also given in this section. This analysis points out the effect of the elongational properties upon the energy loss in the entrance region. Section 4 finishes with a study of the elongation rate and first normal stress difference along the axis of symmetry.

2. Phan-Thien–Tanner models

We split the Cauchy stress tensor into a spherical part $p\mathbf{I}$, a Newtonian contribution, with a first viscosity η_n , and an extra-stress component $\boldsymbol{\tau}$:

$$\boldsymbol{\sigma} = -p\mathbf{I} + 2\eta_n D(\mathbf{u}) + \boldsymbol{\tau}, \tag{1}$$

where $D(\mathbf{u}) = (1/2)(\nabla\mathbf{u} + \nabla\mathbf{u}^t)$ denotes the rate-of-deformation tensor. The extra-stress component $\boldsymbol{\tau}$ satisfies a constitutive equation. In the exponential version of the Phan-Thien–Tanner model, a material parameter ϵ of the model is introduced:

$$\lambda \overset{\square}{\boldsymbol{\tau}} + \exp\left(\frac{\epsilon\lambda}{\eta_v} \text{tr } \boldsymbol{\tau}\right) \boldsymbol{\tau} = 2\eta_v D(\mathbf{u}), \tag{2}$$

where λ is the time-relaxation parameter and η_v is a second viscosity. The linear version introduces a linear term instead of the exponential one:

$$\lambda \overset{\square}{\boldsymbol{\tau}} + \left(1 + \frac{\epsilon\lambda}{\eta_v} \text{tr } \boldsymbol{\tau}\right) \boldsymbol{\tau} = 2\eta_v D(\mathbf{u}). \tag{3}$$

The material derivative ($\overset{\square}{\cdot}$) in (2) and (3) is defined by

$$\overset{\square}{\boldsymbol{\tau}} = \frac{\partial \boldsymbol{\tau}}{\partial t} + \mathbf{u} \cdot \nabla \boldsymbol{\tau} + \beta_a(\boldsymbol{\tau}, \nabla \mathbf{u}), \tag{4}$$

where the bilinear form $\beta_a(\cdot, \cdot)$ is given by

$$\beta_a(\boldsymbol{\tau}, \nabla \mathbf{u}) = -W(\mathbf{u}) \cdot \boldsymbol{\tau} + \boldsymbol{\tau} \cdot W(\mathbf{u}) - a(D(\mathbf{u}) \cdot \boldsymbol{\tau} + \boldsymbol{\tau} \cdot D(\mathbf{u})). \tag{5}$$

$a \in [-1, 1]$ is a material parameter and $W = (1/2)(\nabla\mathbf{u} - \nabla\mathbf{u}^t)$ is the vorticity tensor.

2.1 Shear and elongational viscosities

The present section shows the sensitivity of steady shear and elongational viscosities to the variations of the material parameters ϵ , a , and $\alpha = \eta_v/\eta_0$, where $\eta_0 = \eta_n + \eta_v$.

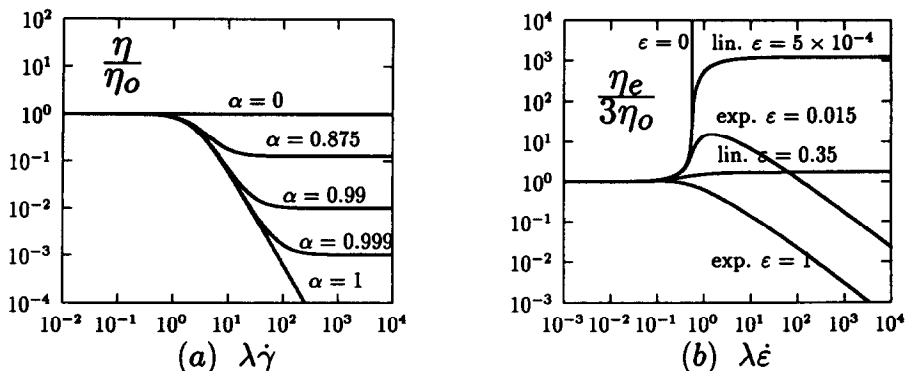


Fig. 1. Simple flows: (a) shear viscosity ($\epsilon = 0.015$, $a = 0.9$, exponential version); (b) elongational viscosity ($\alpha = 0.875$, $a = 0.9$).

The shear viscosity η is a decreasing function of the shear rate $\dot{\gamma}$ (Fig. 1(a)). For high values of shear rate, the steady shear viscosity is mainly governed by α . When α vanishes, $\eta = \eta_0$, and the behavior is Newtonian. When $0 < \alpha < 1$, η tends to a plateau. The asymptotical value of the plateau depends strongly upon α . A large amount of shear-thinning appears at the vicinity of $\alpha = 1$. For $\alpha = 1$, η tends to zero for high values of $\dot{\gamma}$, and the model is Maxwell-like. The material parameters a and ϵ and the model family (exponential or linear) have little impact upon η outside the vicinity of the Oldroyd-B model ($a = 1$ and $\epsilon = 0$).

In the case of the exponential Phan-Thien–Tanner model, the elongational viscosity η_e , as a function of the elongational rate $\dot{\epsilon}$, reaches a maximum, and decreases for high values of $\dot{\epsilon}$ (Fig. 1(b)). For the linear version, η_e increases monotonically with $\dot{\epsilon}$, and tends to a plateau. When ϵ vanishes, the Johnson–Segalman model is obtained: η_e becomes infinite for a finite value of $\dot{\epsilon}$. The material parameters a and α have very little impact upon η_e outside the vicinity of the Oldroyd-B model.

2.2 Dimensionless numbers

Since the shear rate at the downstream wall $\dot{\gamma}_w$ takes large values for shear-thinning fluid models in contractions, we introduce an average value $\overline{\dot{\gamma}_w}$ (overlined), defined by

$$\overline{\dot{\gamma}_w} = \frac{4Q}{\pi r_0^3}.$$

Q is the flow rate, and r_0 is the downstream channel radius.

The Weissenberg number We is defined in an abrupt contraction by [1]

$$We = \frac{N_1|_{\dot{\gamma}=\overline{\dot{\gamma}_w}}}{\sigma_{rz}|_{\dot{\gamma}=\overline{\dot{\gamma}_w}}}, \tag{6}$$

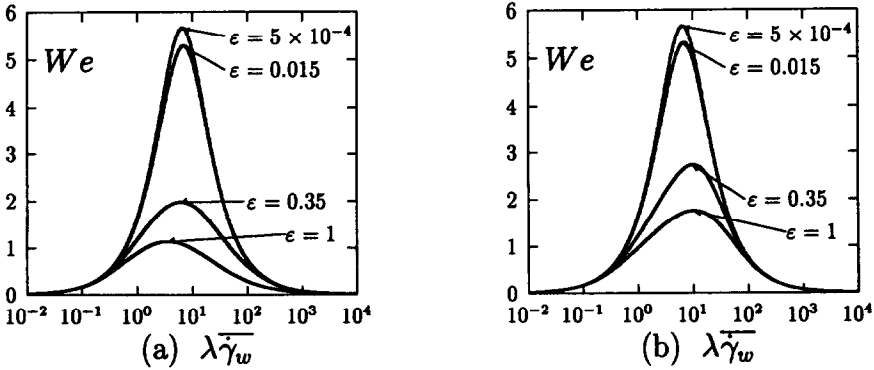


Fig. 2. Weissenberg number: (a) exponential version, and (b) linear version ($\alpha = 0.875$, $a = 0.9$).

where N_1 is the first normal stress difference in shear, σ_{rz} the total shear stress in shear. Figure 2 shows the variations of We versus $\lambda\dot{\gamma}_w$. For both the exponential and the linear versions, We presents a maximum and decreases for high values of $\lambda\dot{\gamma}_w$. We will see in section 4 that these variation are not correlated to vortex enhancements.

Let X_E be the following dimensionless number:

$$X_E = \log_{10} \left(\frac{\sigma_{E|e=\dot{\gamma}_w}}{3\sigma_{rz|\dot{\gamma}_w}} \right), \tag{7}$$

where σ_E is the first normal stress difference in uniaxial extension. Figure 3 shows the variations of X_E versus $\lambda\dot{\gamma}_w$. For the exponential version (Fig. 3(a)), X_E shows a maximum, and decreases for high values of $\lambda\dot{\gamma}_w$. For the linear version (Fig. 3(b)), X_E increases with $\lambda\dot{\gamma}_w$, and tends to a plateau. We

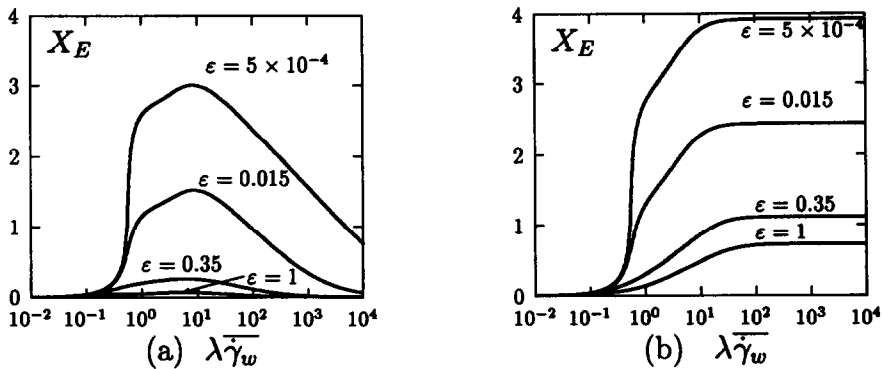


Fig. 3. Dimensionless X_E number: (a) exponential version and, (b) linear version ($\alpha = 0.875$, $a = 0.9$).

will see in section 4 that the variations of X_E correspond to the vortex developments. For the exponential version, vortex size and intensity as a function of $\lambda\dot{\gamma}_w$, increase, reach a maximum, and then decrease. For the linear version, vortex size and intensity reach a plateau for high values of $\lambda\dot{\gamma}_w$.

In fact, definition (7) takes into account the elongational properties of the models, while the expression (6) for We only contains shear properties. Note that X_E can be expressed by using the Trouton ratio $X_E = \log_{10}(\eta_e/3\eta)$ and takes advantage of the \log_{10} function to reduce the range of $\eta_e/3\eta$.

3. Numerical method

We introduce in this paragraph the partial derivative formulation of the problem and the numerical strategy. The set of equations contains the constitutive eqn. (8), the conservation of momentum (9), and the conservation of mass (10):

$$\frac{\lambda}{2\eta_v} \tau + \frac{f(\tau)}{2\eta_v} \tau - D(\mathbf{u}) = 0, \tag{8}$$

$$-\rho \left(\frac{\partial \mathbf{u}}{\partial t} + \mathbf{u} \cdot \nabla \mathbf{u} \right) + \text{div } \tau + \eta_n \Delta \mathbf{u} - \nabla p = 0, \tag{9}$$

$$\text{div } \mathbf{u} = 0. \tag{10}$$

We add initial conditions for τ and \mathbf{u} , boundary conditions for \mathbf{u} , and upstream boundary conditions for τ . The inertia term $\mathbf{u} \cdot \nabla \mathbf{u}$ is neglected in (9), since only slow flows are investigated. The material function $f(\tau)$ switches between the two versions of the Phan-Thien–Tanner model:

$$f(\tau) = \begin{cases} \exp\left(\frac{\epsilon\lambda}{\eta_v} \text{tr}\tau\right) \\ \text{or} \\ 1 + \frac{\epsilon\lambda}{\eta_v} \text{tr } \tau. \end{cases}$$

3.1 Operator splitting

Let $T(\mathbf{u})$ be the stress transport operator: $T(\mathbf{u})\tau = \mathbf{u} \cdot \nabla \tau + \beta_\alpha(\tau, \nabla \mathbf{u})$.

Let A be the following operator:

$$A(\tau, \mathbf{u}, p) = \begin{bmatrix} \frac{\lambda}{2\eta_v} T(\mathbf{u})\tau + \frac{f(\tau)}{2\eta_v} \tau - D(\mathbf{u}) \\ \text{div } \tau + \eta_n \Delta \mathbf{u} - \nabla p \\ \text{div } \mathbf{u} \end{bmatrix} \tag{11}$$

associated with the boundary conditions for τ and \mathbf{u} . As mentioned above, the inertia term $\mathbf{u} \cdot \nabla \mathbf{u}$ is neglected in (11).

Let m be the constant diagonal matrix: $m = \text{diag}(\lambda/2\eta_v, -\rho, 0)$.

The problem can be rewritten in a more compact way:

(P): Find $\mathcal{U} = (\tau, \mathbf{u}, p)$ such that

$$m \frac{\partial \mathcal{U}}{\partial t} + A(\mathcal{U}) = 0 \tag{12}$$

We propose a time-approximation of problem (P). Our goal is here to obtain fast convergence to stationary solutions. We use an operator splitting procedure [12, 13]:

$$A = A_1 + A_2, \tag{13}$$

where A_1 contains the elliptic part of the operator A , and A_2 the hyperbolic non-linear part [10, 11, 14].

3.2 Time approximation

Using results of operator splitting procedure, we solve problem (P) by a three-step algorithm:

$(P)_{\Delta t}$: \mathcal{U}_0 given;

$n \geq 0$, \mathcal{U}^n being known, find \mathcal{U}^{n+1} such that

$$m \frac{\mathcal{U}^{n+\theta} - \mathcal{U}^n}{\theta \Delta t} + A_1(\mathcal{U}^{n+\theta}) = -A_2(\mathcal{U}^n), \tag{14}$$

$$m \frac{\mathcal{U}^{n+1-\theta} - \mathcal{U}^{n+\theta}}{(1-2\theta) \Delta t} + A_2(\mathcal{U}^{n+1-\theta}) = -A_1(\mathcal{U}^{n+\theta}), \tag{15}$$

$$m \frac{\mathcal{U}^{n+1} - \mathcal{U}^{n+1-\theta}}{\theta \Delta t} + A_1(\mathcal{U}^{n+1}) = -A_2(\mathcal{U}^{n+1-\theta}), \tag{16}$$

where Δt is the time step and θ is a parameter of the method (see Fig. 4).

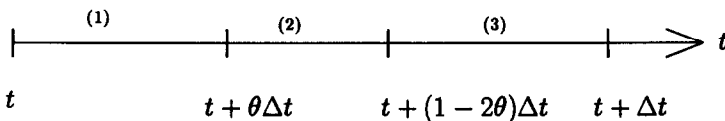


Fig. 4. Time-approximation by using a θ -method.

This algorithm enables us to split up the two main difficulties of the problem, i.e. the non-linearity of the constitutive equation (8) and the incompressibility relation (10). The choice of the time-step Δt is related to a conditional stability condition [11,15].

Furthermore, this time-approximation leads to fast convergence to stationary solutions [10,14]. The criteria for determining that a steady state solution is reached, is related to the discrete L^2 -norm of the stationary solution $A(\mathcal{U}) = 0$.

3.3 Finite element method

We use here the light element proposed in [10,11] (see also Fig. 5). This element leads to roughly ten times smaller non-linear systems than the other elements [16, 17]. It is a combination of the Raviart–Thomas [18] element for the velocity–pressure field, a P_0 discontinuous element for normal stress components, and a linear continuous element for the shear stress components (see Fig. 5). Note that this finite element method appears as an extension of a Marker and Cell finite difference scheme.

We use an upwinding scheme for the stress transport term $\mathbf{u} \cdot \nabla \boldsymbol{\tau}$ in (8). We develop the Lesaint–Raviart scheme [19] for the normal stress components, and the Baba–Tabata scheme [20] for the shear stress components. These two schemes are Total Variation Decreasing. This property guarantees non-artificial oscillating solutions, as shown in paragraph 3.5 for profile along the axis of symmetry. We refer also to [14] for a study of this numerical technique and related results for stresses at the vicinity of the reentrant corner.

Note that the SUPG and the SU methods [11,16,21] do not guarantee this property (see also Ref. 22).

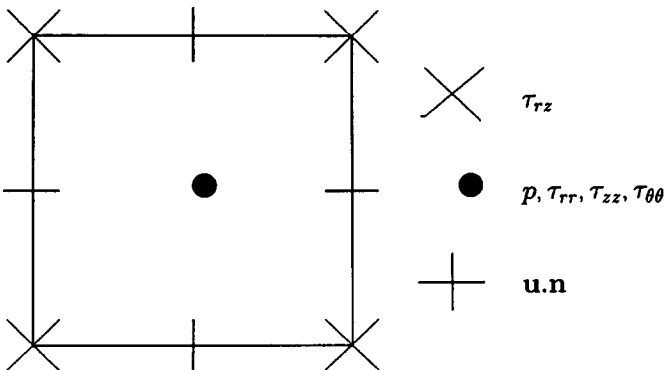


Fig. 5. Finite element method.

4. Numerical experiments in an 8:1 abrupt contraction

In the present section, we wish to investigate the linear and the exponential version of the Phan–Thien–Tanner model. An axisymmetric 8:1 abrupt contraction is considered. The material parameters are $\eta_v/\eta_0 = 0.875$ and $a = 0.9$. For the exponential version, we choose $\epsilon = 1$ (tiny elongational effects) and $\epsilon = 0.015$ (large effects), and for the linear version $\epsilon = 0.35$ (tiny effects). $\epsilon = 5 \times 10^{-4}$ (large effects).

As the boundary condition are concerned, we consider Poiseuille flows at upstream and downstream sections, a symmetry condition along the axis, and $\mathbf{u} = 0$ at the wall.

Starting from a Newtonian solution, a branch of viscoelastic solutions is computed by using a continuation process. The parameter of command is $\lambda\dot{\gamma}_w$ during the computation. This parameter increases with the flow rate Q and with the time relaxation parameter λ .

4.1 Finite element meshes

Two finite element meshes (Fig. 6) of domain Ω are considered for the study of this section. They have in common entry and exit lengths respec-

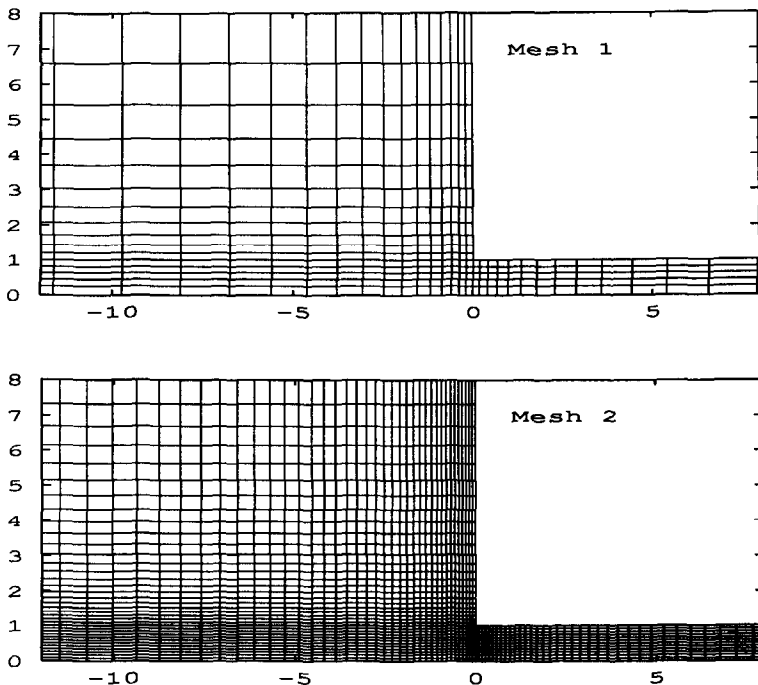


Fig. 6. Partial view of the finite element meshes.

Table 1
Relevant data for the finite element meshes

Mesh	Number of elements	Number of nodes	Number of degrees of freedom	Size of the corner element
1	525	592	3810	0.16
2	3264	3445	23211	0.08

tively equal to 64 and 150 radii. Both upstream and downstream lengths are sufficiently long so that fully developed conditions can exist. Mesh 1 is coarse and is useful to experiment models and test convergence with mesh refinement. Mesh 2 present a quasi-regular spacing in the entry region (axial and radial directions). Relevant data about these meshes are summarized in Table 1.

4.2 Flow Patterns

Let us observe the flow pattern versus the command parameter $\lambda\dot{\gamma}_w$. Figure 7(a) shows the Newtonian behavior. A small vortex is present in the salient corner of the contraction.

The set of pictures in Fig. 7 shows the evolution of the exponential model with $\epsilon = 0.015$. The elongational viscosity reaches a maximum and tends to zero for high ratios of the elongational rate (see Fig. 1(b)). For small values of $\lambda\dot{\gamma}_w$, the vortex develops from the salient corner to the reentrant corner (Fig. 7(b)). When $\lambda\dot{\gamma}_w$ increases, the vortex grows in intensity, and the borderline separating the main flow from the vortices goes from concave to convex (Fig. 7(c)). For higher values of $\lambda\dot{\gamma}_w$, the vortex size increases rapidly and the vortex develops in the upstream domain. The maximum vortex intensity, i.e. the ratio of the recirculating flow rate to the main flow rate, reaches a maximum for $\lambda\dot{\gamma}_w = 42$ (Fig. 7(d)) while its maximum size is reached for $\lambda\dot{\gamma}_w = 206$ (Fig. 7(e)). For higher values of $\lambda\dot{\gamma}_w$, the vortex decreases slowly in size and intensity (Fig. 7(f)). We refer also to [14, 23] for numerical experiments of the exponential Phan-Thien–Tanner model in a 4:1 abrupt contraction.

Let us now consider the exponential model with $\epsilon = 1$. We get a monotonically decreasing elongational and shear viscosity (see Fig. 1(a) and 1(b)). Figure 8 show that the vortex decreases in size and intensity for high values of $\lambda\dot{\gamma}_w$, and becomes smaller than for a Newtonian fluid.

A second approach to elongational effects can be obtained by using the linear model with $\epsilon = 5 \times 10^{-4}$. The elongational viscosity is an mono-

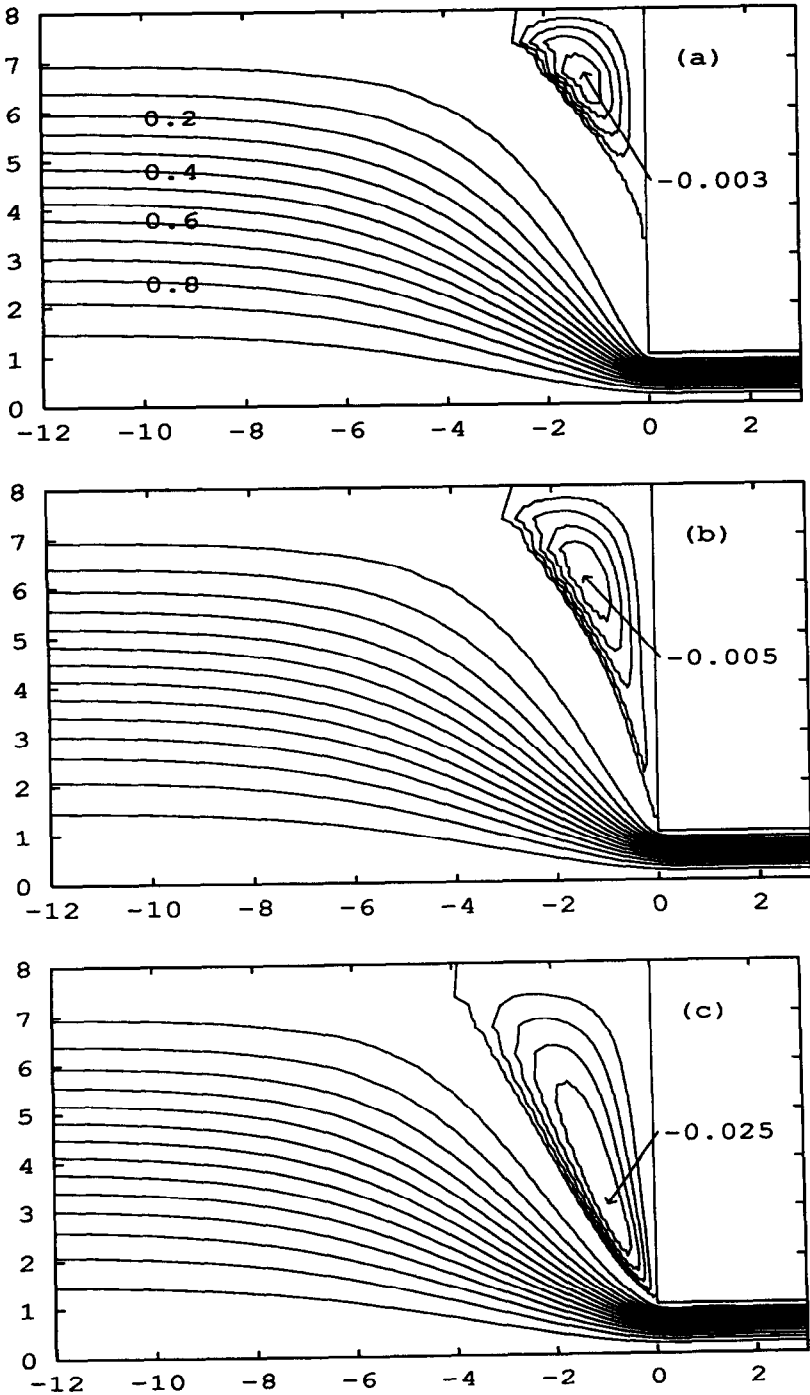


Fig. 7 (a-c).

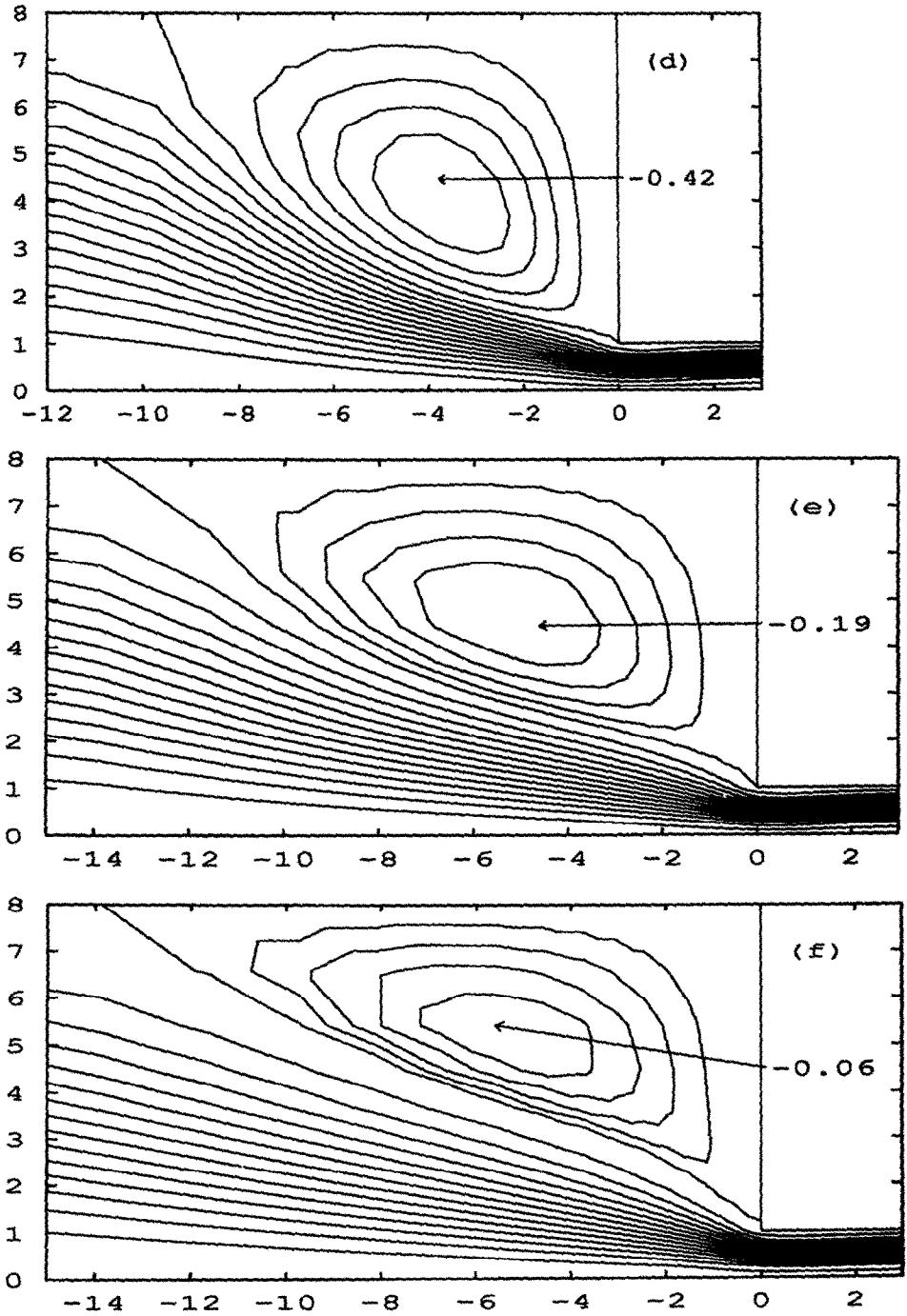


Fig. 7. Exponential version ($\epsilon = 0.015$): vortex developments: (a) $\lambda_w = 0$; (b) $\lambda_w = 1.5$; (c) $\lambda_w = 4.5$; (d) $\lambda_w = 42$; (e) $\lambda_w = 206$; (f) $\lambda_w = 626$.

tonically increasing function of $\overline{\lambda\dot{\gamma}_w}$ (see Fig. 1(b)). For small values of $\overline{\lambda\dot{\gamma}_w}$, the situation is comparable with the previous one (exponential version, $\epsilon = 0.015$). When $\overline{\lambda\dot{\gamma}_w}$ increases, the vortex grows in intensity (Fig. 9(a)), and we observe also the change of the borderline concavity (Fig. 9(b)). For higher values of $\overline{\lambda\dot{\gamma}_w}$, the vortex develops rapidly in the upstream channel (Fig. 9(c)). The vortex size and activity is a monotonically increasing function of $\overline{\lambda\dot{\gamma}_w}$, and tends slowly to an asymptotical behavior (Fig. 9(d)). Note also the movement of the vortex center from the salient corner region (Fig. 9(a)) to the vicinity of the reentrant corner (Fig. 9(b)) and then upstream (Fig. 9(c) and 9(d)). See Refs. 2, 24–26 for related experiments with real fluids.

Finally, the linear model with $\epsilon = 0.35$ is considered. The vortex develops from the salient corner to the reentrant corner of the contraction (Fig. 10(a)). The vortex intensity reaches a maximum for $\overline{\lambda\dot{\gamma}_w} = 77$ (Fig. 10(b)). For higher values of $\overline{\lambda\dot{\gamma}_w}$, the vortex size continues to increase, and tends slowly to asymptotical behavior (Fig. 10(c) and 10(d)).

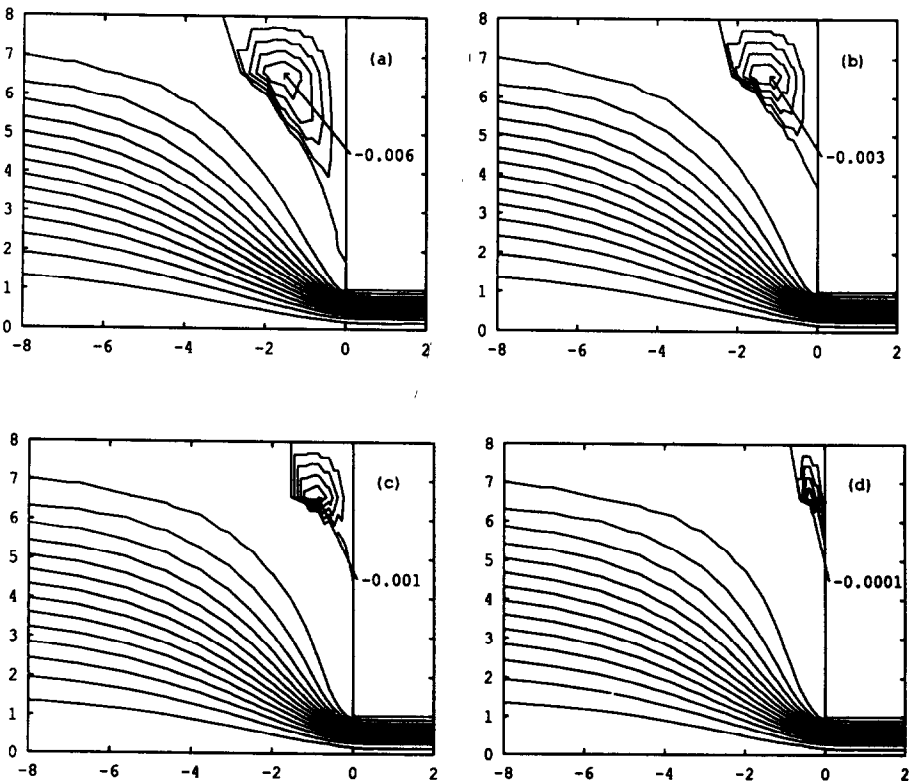


Fig. 8. Exponential version ($\epsilon = 1$): vortex developments: (a) $\overline{\lambda\dot{\gamma}_w} = 4$; (b) $\overline{\lambda\dot{\gamma}_w} = 19$; (c) $\overline{\lambda\dot{\gamma}_w} = 52$; (d) $\overline{\lambda\dot{\gamma}_w} = 182$.

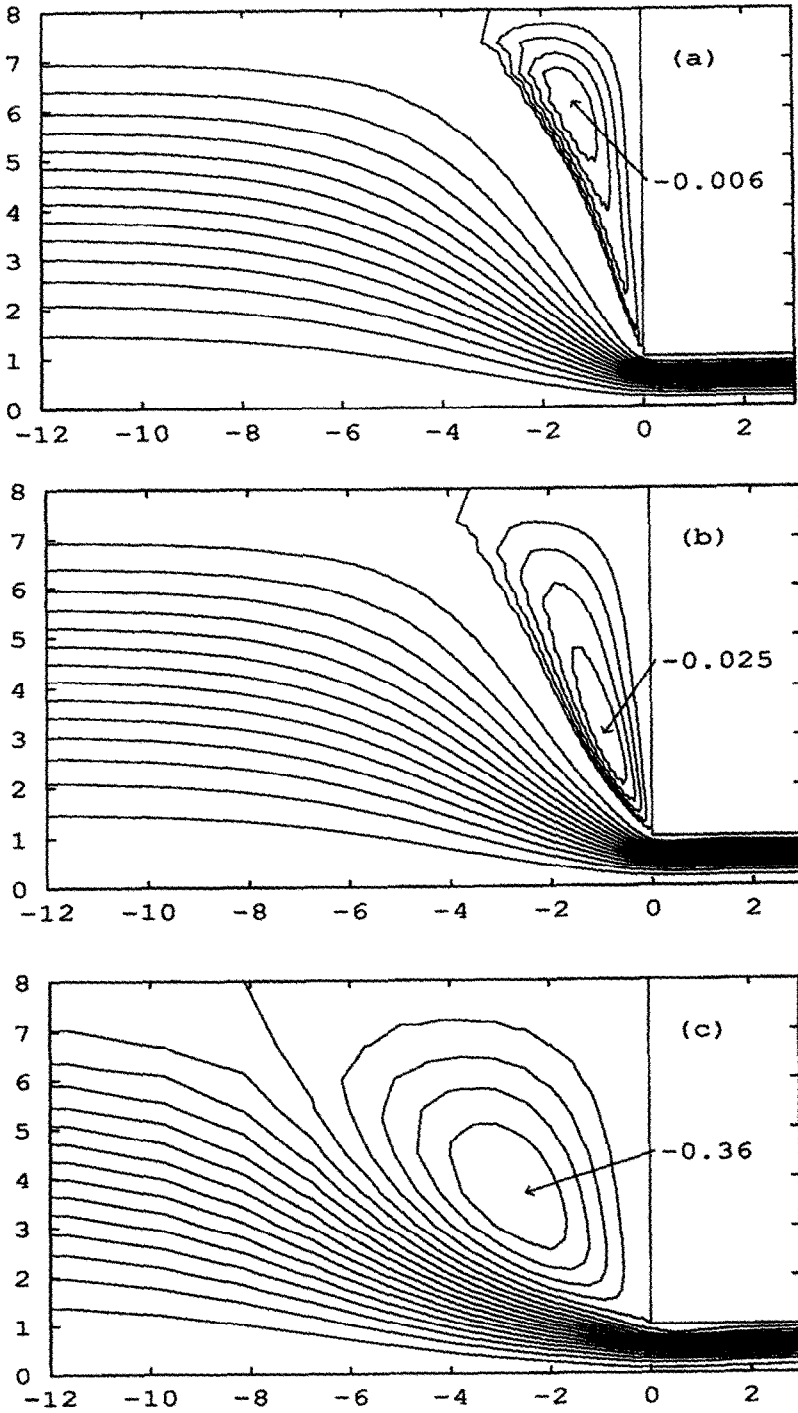


Fig. 9(a-c).

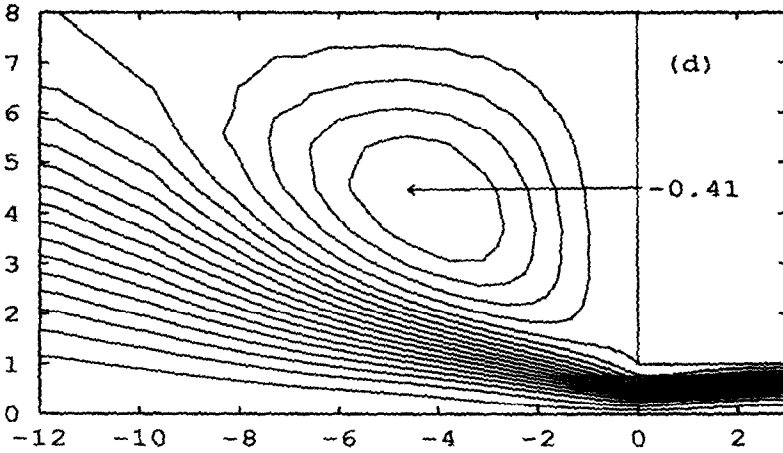


Fig. 9. Linear version ($\epsilon = 5 \times 10^{-4}$); vortex developments: (a) $\lambda\dot{\gamma}_w = 2.0$; (b) $\dot{\gamma}_w = 4.6$; (c) $\lambda\dot{\gamma}_w = 14$; (d) $\lambda\dot{\gamma}_w = 69$.

4.3 Vortex activity and reattachment length

Figure 11 shows the vortex activity for the various fluids under consideration. Vortex activity is considered as a function of both $\lambda\dot{\gamma}_w$ and X_E . For small values of $\dot{\gamma}_w$, the vortex activity is an increasing function of $\dot{\gamma}_w$ (Fig. 11, first column). For large values of $\dot{\gamma}_w$, exponential and linear versions exhibit different asymptotical behaviors. In the exponential case (Fig. 11(a) and 11(b)), the vortex activity decreases. This is not surprising, since η_e asymptotically decreases too. In the linear case (Fig. 11(c) and 11(d)), as expected, the vortex activity tends to an asymptotical value, while η_e reaches

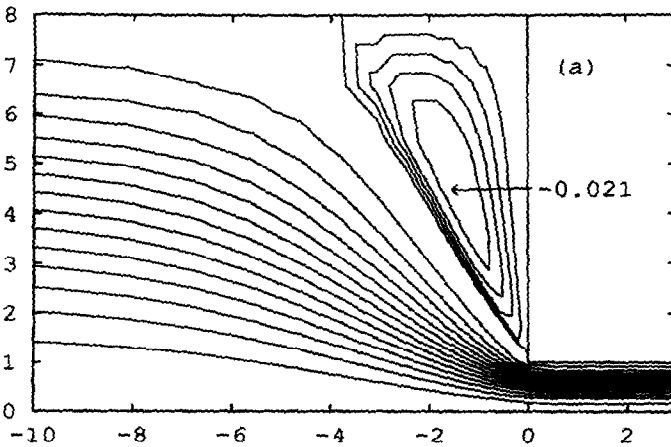


Fig. 10(a).

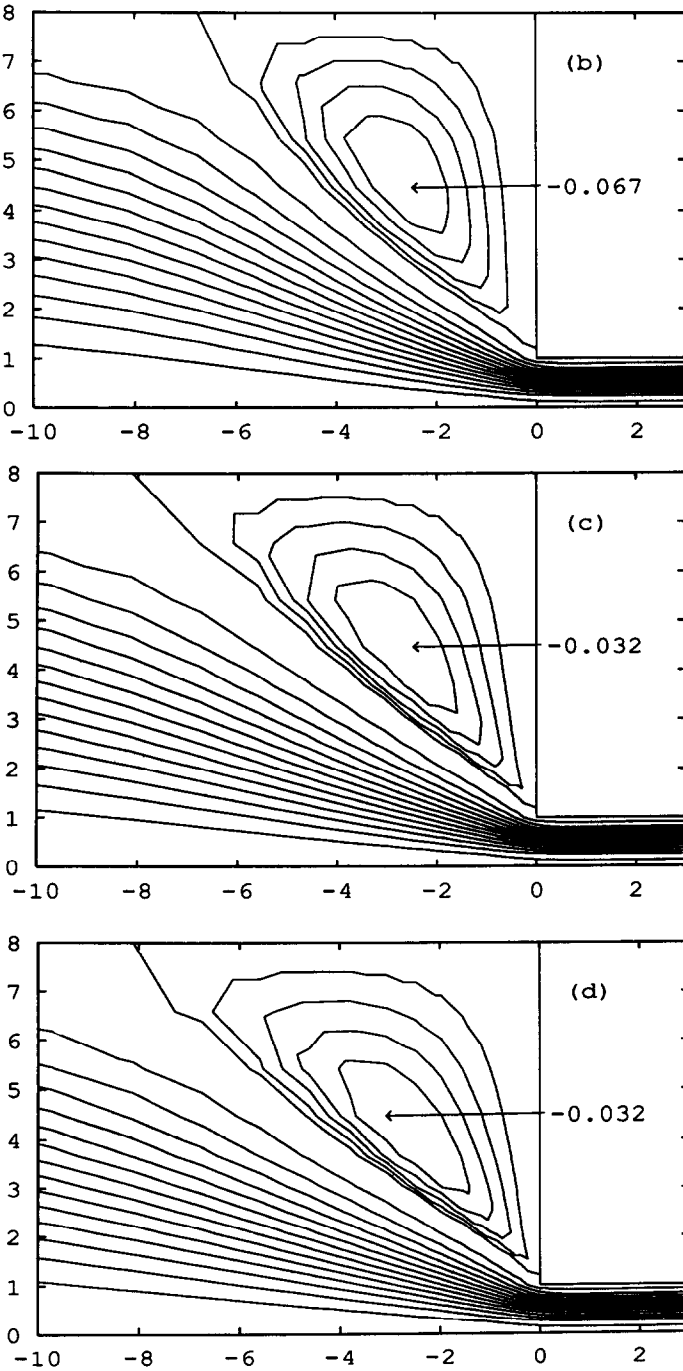


Fig. 10. Linear version ($\epsilon = 0.35$): vortex developments. (a) $\lambda \bar{\dot{\gamma}}_w = 7$; (b) $\lambda \bar{\dot{\gamma}}_w = 77$; (c) $\lambda \bar{\dot{\gamma}}_w = 768$; (d) $\lambda \bar{\dot{\gamma}}_w = 1667$.

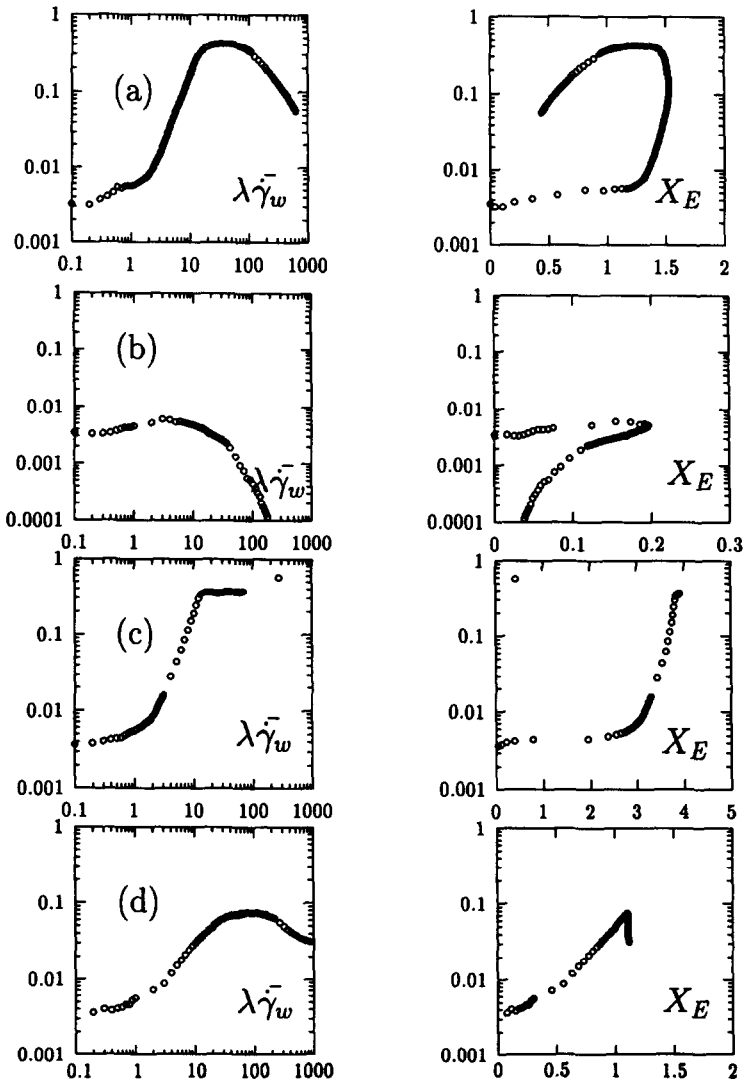


Fig. 11. Vortex activity: exponential version: (a) $\epsilon = 0.015$, (b) $\epsilon = 1$; linear version: (c) $\epsilon = 5 \times 10^{-4}$, (d) $\epsilon = 0.35$.

a plateau. Note the logarithmic scale used for $\overline{\dot{\gamma}_w}$. The second column of Fig. 11 uses X_E to show in a dimensionless way the correlation between the variations of the vortex activity and the elongational effects. In the exponential case, the curves go back to the origin, and in the linear case, a fixed point is reached. While elongational effects and vortex activity are clearly correlated, no simple analytic law can yet be deduced. The vortex development phenomena appears as a complex one.

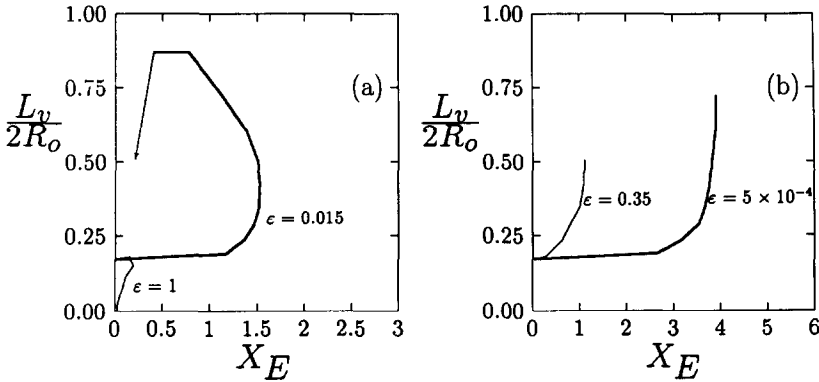


Fig. 12. Reattachment length: (a) exponential version; (b) linear versions

Let L_v be the reattachment length and R_0 the upstream channel radius. The dimensionless quantity $L_v/2R_0$ as a function of X_E is reproduced in Fig. 12. Significant vortex growth is generated for the exponential and linear version both for small values of ϵ (exponential version $\epsilon = 0.015$ (Fig. 12(a)), and linear version $\epsilon = 5 \times 10^{-4}$ (Fig. 12(b)). The linear version with $\epsilon = 0.35$ shows moderate vortex growth (Fig. 12(b)). We refer to Ref. 24, p. 173 for related results with polymer solutions. The exponential model with $\epsilon = 1$ point out shear-thinning effects. As expected, the vortex reattachment length is decreasing.

Note that the ratio $L_v/2R_0$ takes the Newtonian value 0.17 associated with $X_E = 0$. For the exponential model at high values of $\lambda\dot{\gamma}_w$, the elongational properties become negligible, and the shear properties are predominant (see also Fig. 1). As a consequence, the ratio η_e/η and X_E decrease when $\lambda\dot{\gamma}_w$ becomes large. As expected, the vortex size reaches a maximum and start to decrease, according to the variation of X_E (Fig. 12(a)). For the linear model, the elongational and shear viscosities tend to constant values when $\lambda\dot{\gamma}_w$ becomes large. Thus, X_E tends to a constant. According to this prediction, the vortex reattachment length tends to a constant at high values of $\lambda\dot{\gamma}_w$ (Fig. 12(b)).

4.4 Pressure drop in the entrance

The total pressure drop in the flow domain Ω is given by

$$\Delta p(\Omega; \tau, \mathbf{u}) = -\frac{2\pi}{Q} \int_{\Gamma} (\mathbf{u} \cdot \mathbf{n}) p \, ds, \quad (17)$$

where Q is the flow rate, and \mathbf{n} the outward unit normal onto the boundary $\Gamma = \partial\Omega$ of Ω . According to Green's formula, the sum over Γ in (17) can be

also expressed as

$$\int_{\Gamma} (\mathbf{u} \cdot \mathbf{n})p \, ds = \int_{\Omega} \mathbf{u} \cdot \nabla p \, dx,$$

since $\text{div } \mathbf{u} = 0$.

The solution is assumed to be stationary ($\partial \mathbf{u} / \partial t = 0$). The conversion of momentum (9) leads to $\nabla p = \text{div}(2\eta_n D(\mathbf{u}) + \boldsymbol{\tau})$ since only slow flows are considered (the inertia term $\mathbf{u} \cdot \nabla \mathbf{u}$ is neglected).

By using a second integration by part, (17) becomes

$$\begin{aligned} \Delta p(\Omega; \boldsymbol{\tau}, \mathbf{u}) &= \frac{2\pi}{Q} \int_{\Omega} D(\mathbf{u}) : (2\eta_n D(\mathbf{u}) + \boldsymbol{\tau}) \, dx \\ &\quad - \frac{2\pi}{Q} \int_{\Gamma} (2\eta_n D(\mathbf{u}) + \boldsymbol{\tau}) : (\mathbf{u} \otimes \mathbf{n}) \, ds, \end{aligned} \tag{18}$$

where $\mathbf{u} \otimes \mathbf{n} = (u_i n_j)_{i,j}$ denotes the tensorial product of the two vectors \mathbf{u} and \mathbf{n} .

The pressure drop associated with the fully developed Poiseuille flow is defined by

$$\Delta p_i = \Delta p(\Omega_i; \boldsymbol{\tau}_i, \mathbf{u}_i), \quad 1 \leq i \leq 2,$$

where Ω_1 (resp. Ω_2) is the upstream (resp. downstream) channel, and $\boldsymbol{\tau}_1, \mathbf{u}_1$ (resp. $\boldsymbol{\tau}_2, \mathbf{u}_2$) the fully developed Poiseuille flow at upstream (resp. downstream).

Following Ref. 24, we define the energy loss in the entrance region of the contraction by taking away the energy loss caused by the Poiseuille flow from the total energy loss in the contraction:

$$\Delta p_{\text{en}} = \Delta p(\Omega; \boldsymbol{\tau}, \mathbf{u}) - \sum_{i=1}^2 \Delta p_i.$$

As specified in paragraph 4.1, both upstream and downstream lengths are sufficiently long so that fully developed conditions can exist. This property guarantees that Δp_{en} is independent of the length of both upstream and downstream domains.

The Couette correction (C) is given by

$$C = \frac{\Delta p_{\text{en}}}{2\eta_0 \dot{\gamma}_w}. \tag{19}$$

The Couette correction expresses (in a dimensionless way) the energy loss in the entrance region.

Since Δp_{en} depends on the dimension of our system, a dimensionless version of this quantity is introduced:

$$\delta p_{\text{en}} = \frac{\lambda}{2\eta_0} \Delta p_{\text{en}} = \lambda \overline{\dot{\gamma}_w} C. \tag{20}$$

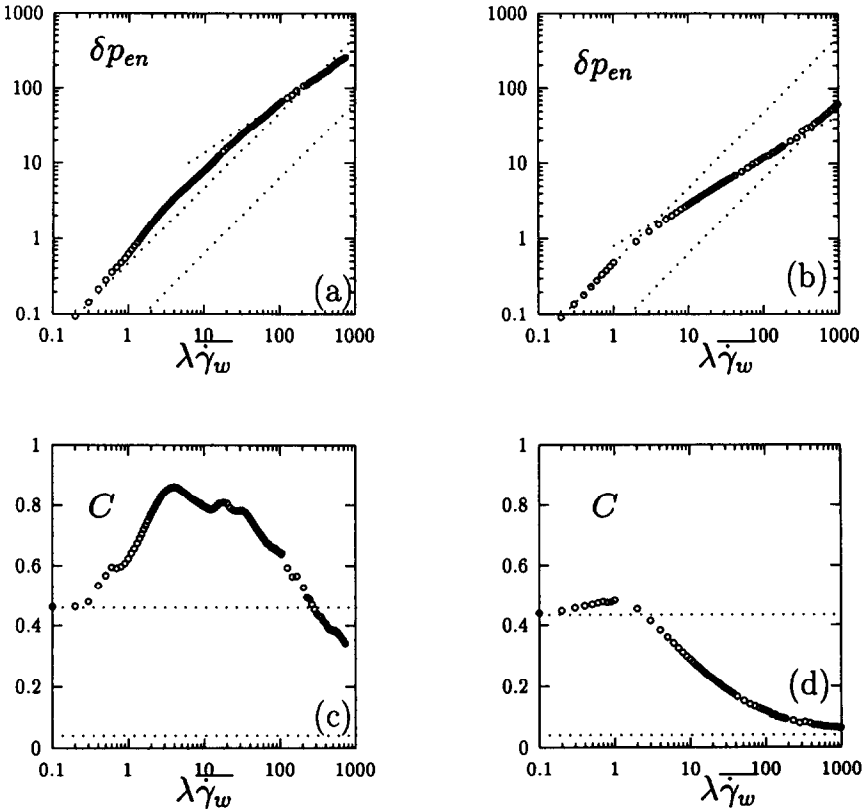


Fig. 13. Exponential version: pressure drop: (a) $\epsilon = 0.015$, (b) $\epsilon = 1$; Couette correction: (c) $\epsilon = 0.015$, (d) $\epsilon = 1$.

Figures 13 and 14 plot δp_{en} and C versus $\lambda \dot{\gamma}_w$. For both the exponential version (Fig. 13) and the linear version (Fig. 14), different flow regimes can be observed. The first flow regime is Newtonian-like. The flow curves on Figs. 13(a), 13(b), 14(a), and 14(b) exhibit a slope of 1, and $\delta p_{en} = C_0 \lambda \dot{\gamma}_w$ for small values of $\lambda \dot{\gamma}_w$, where $C_0 = 0.46$.

For high values of $\lambda \dot{\gamma}_w$, the flow curves also show a slope of 1, and $\delta p_{en} = C_\infty \lambda \dot{\gamma}_w$, except on Fig. 13(a), where the asymptotical behavior is still not reached. In this case, the expected asymptote for very high values of $\lambda \dot{\gamma}_w$ is indicated by a dotted line. Note that C_∞ depends on the material parameters of the model, while C_0 is constant.

The intermediate flow regime presents roughly a power law character: δp_{en} is proportional to $(\lambda \dot{\gamma}_w)^k$. The linear case with $\epsilon = 5 \times 10^{-4}$ shows $k > 1$. We refer to Refs 26, 27 for the experimental study and the modeling of the pressure drop associated with solutions in thick solvents. We point

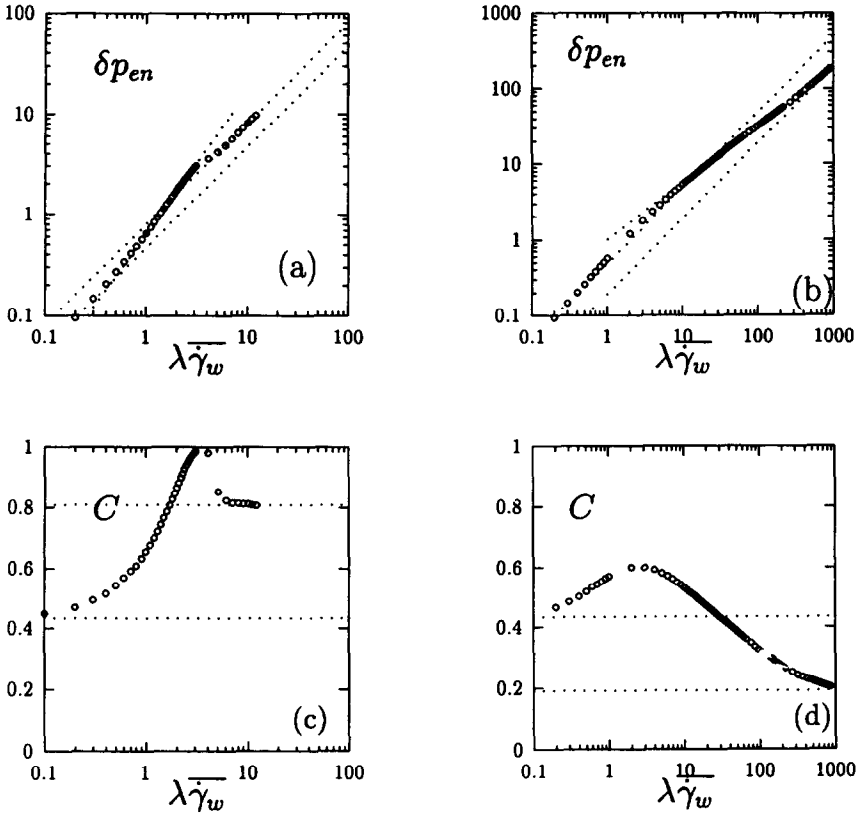


Fig. 14. Linear version: pressure drop: (a) $\epsilon = 5 \times 10^{-4}$, (b) $\epsilon = 0.35$; Couette correction: (c) $\epsilon = 5 \times 10^{-4}$, (d) $\epsilon = 0.35$.

out that the behaviors of Phan-Thien–Tanner fluids are qualitatively in good agreement with experimental measurements. The linear version can be associated with polymer solutions, while the exponential one reflects more polymer melt-like behavior.

The Couette correction on Figs. 13 and 14 presents some details of the pressure drop in the entrance region. For the exponential version $\epsilon = 0.015$, the dependence of C on $\lambda \dot{\gamma}_w$ is complex (Fig. 13(c)). Asymptotically, for very high values of $\lambda \dot{\gamma}_w$, we expect an asymptotical value of C (in dotted lines). Using the exponential Phan-Thien–Tanner model in a 4:1 circular abrupt contraction, Debbaut et al. [23] report the C decreases very slightly before increasing to a maximum of approximately 3.75 at $\lambda \dot{\gamma}_w \approx 2.5$ before decreasing again. Note that the “Weissenberg number” introduced in [23], denoted here We^* , is given by $We^* = \lambda \dot{\gamma}_w / 4$.

Table 2 gives a summary for the values of C_∞ and k , depending on the fluid under consideration. These values are computed by using mesh 1.

Table 2

Flow regimes: Phan-Thien–Tanner models

C_∞	k	Model version	ϵ
0.04?	0.67	exponential	0.015
0.04	0.58	exponential	1
0.81	1.40	linear	5×10^{-4}
0.19	0.75	linear	0.35

Calculations with mesh 2 show that the behavior of C as a function of $\lambda\bar{\gamma}_w$ remains the same (see Fig. 15). Values differ by about 11% of the maximum value, and $C_o = 0.51$ on mesh 2. These values are in semi-quantitative agreement with the results of Coates et al. [28, p. 183], where $C_o \approx 0.57$ with two different meshes on a 8:1 abrupt contraction. Finally, using two meshes of a 4:1 contraction, Debbaut et al. [23] report a 10% change in the maximum value of C .

4.5 Profiles along the axis of symmetry

The profile along the axis of symmetry are presented in this paragraph for both the exponential ($\epsilon = 0.015$) and the linear ($\epsilon = 5 \times 10^{-4}$) versions. The velocity profile is reproduced in Figs 16(a) and 16(d), where \bar{U} is the average velocity downstream. Note the overshoot of the velocity in the entrance region. The velocity reaches a maximum in the downstream domain.

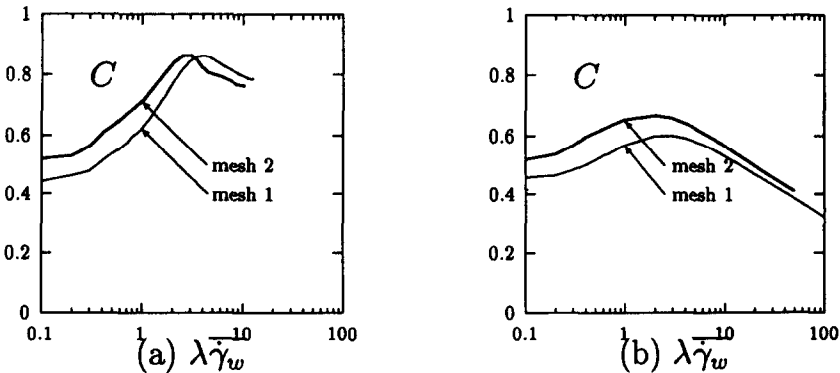


Fig. 15. Mesh sensitivity for the Couette correction: (a) exponential version ($\epsilon = 0.015$); (b) linear version ($\epsilon = 0.35$).

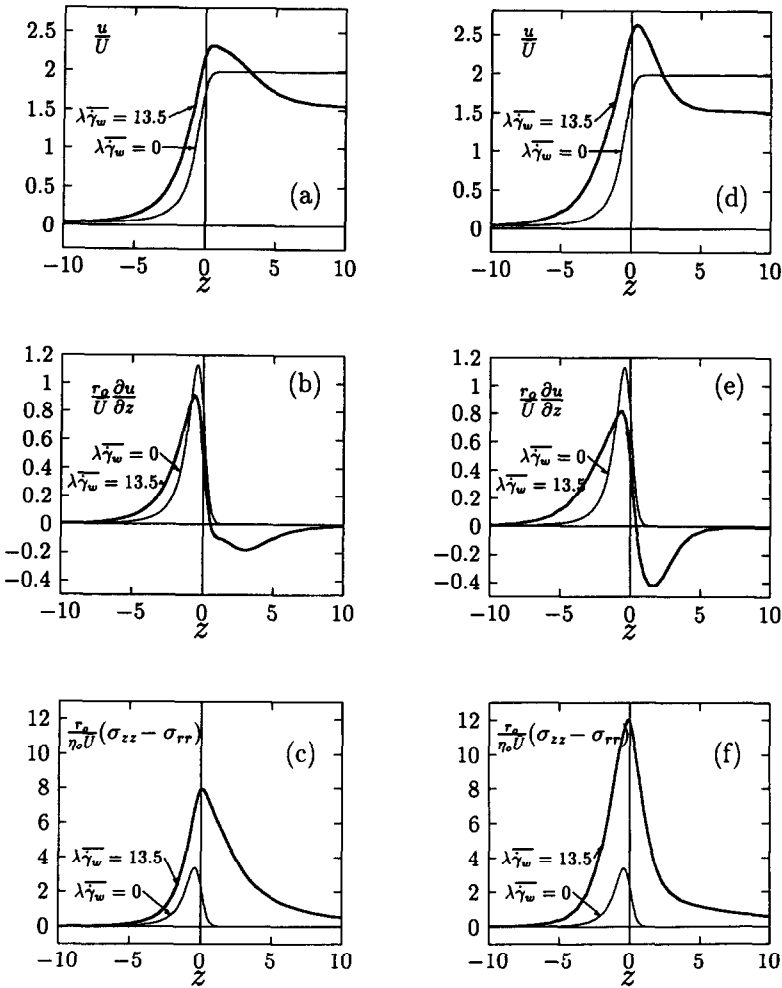


Fig. 16. Profiles along the axis: exponential version $\epsilon = 0.015$, $\lambda\bar{\gamma}_w = 13.5$: (a) velocity; (b) elongational rate; (c) first normal stress difference; linear version $\epsilon = 5 \times 10^{-4}$, $\lambda\bar{\gamma}_w = 13.5$: (d) velocity; (e) elongational rate; (f) first normal stress difference.

Figures 16(b) and 16(e) show the elongational rate along the axis of symmetry ($r = 0$), where r_0 is the downstream channel radius. The Newtonian behavior presents a maximum in the upstream domain near the entry. In the downstream channel, the elongational rate quickly reaches the asymptotical zero value. For the viscoelastic fluid, the maximum goes slightly upstream. The upstream elongation rate is reduced. The elongational rate takes negative values in the downstream channel and slowly reaches the zero value. The change of sign is associated with the overshoot of the velocity.

Figures 16(c) and 16(f) represent the first normal stress difference along the axis of symmetry. The change of scale between the Newtonian and the viscoelastic behavior is here spectacular. The maximum goes slightly downstream, and the relaxation is slower in the viscoelastic case.

5. Conclusions

The objective of this work was to examine the relation between macroscopic features of complex flows in an circular abrupt contraction, such as vortex enhancement, flow curves, velocity gradient, and normal stress difference along the flow axis, and its viscous behavior is simple extensional flows. Since the elongational viscosity of the Phan-Thien–Tanner model is mainly governed by one material parameter, four representative test-fluids have been studied. This model leads to numerical results, such as vortex development and flow curves, that are qualitatively in good agreement with experimental measurements. As previously observed [26,27] with solutions in thick solvents, flow curves here show three flow regimes, and the second one develops a power law character. Moreover, the numerical approach allows a direct access to flow properties, such as elongational rate and first normal stress difference along the axis of symmetry.

The results of the present paper confirm the robustness and the efficiency of the numerical strategy introduced in Refs. 10, 11 and 14. The time dependent approach has allowed us to obtain rapidly stationary solutions of the Phan-Thien–Tanner models. Moreover, the conservative finite element approximation guarantees non-artificial oscillating solutions. An important property of our result is the convergence with the mesh refinement. Macroscopy quantities such as vortex intensity and velocity overshoot (see Ref. 14) show a fast convergence with mesh refinement. The Couette correction reflects some variations between the two meshes of the present study. Values differ by about 11% of the maximum value.

As pointed out by Boger [24], viscoelastic fluid entry flows are not only of interest as an appropriate test problem for developing the fluid mechanics of viscoelastic fluids, but they are also of practical interest and great importance in polymer processing. The ultimate aim is to predict the influence of the entry flow geometry on the kinematics and pressure drop in order both to minimize the latter and optimize the former. Optimization tends to eliminate secondary flows and regions of high stress. Thus, the robustness and efficiency of our approach opens new paths for this prediction of flow phenomena. In addition, complex entry flows appear to be potentially important for viscoelastic fluids rheometrical properties calculations, through the use of appropriate constitutive equations and numerical models.

References

- 1 D.V. Boger, M.J. Crochet, and R.A. Keiller, On viscoelastic flows through abrupt contractions. *J. Non-Newtonian Fluid Mech.*, 44 (1992) 267–279.
- 2 J.M. Piau, N. El Kissi, and B. Tremblay, Low Reynolds number flow visualisation of linear and branched silicones upstream of orifice dies. *J. Non-Newtonian Fluid Mech.*, 30 (1988) 197–232.
- 3 J.M. Piau, N. El Kissi, and B. Tremblay, Influence of upstream instabilities and wall slip on melt fracture and sharkskin phenomena during silicones extrusion through orifice dies, *J. Non-Newtonian Fluid Mech.*, 34 (1990) 145–180.
- 4 R. Keunings and M.J. Crochet, *J. Non-Newtonian Fluid Mech.*, 14 (1984) 279–299.
- 5 S.A. White, A.D. Gotsis, and D.G. Baird, *J. Non-Newtonian Fluid Mech.*, 24 (1987) 121–160.
- 6 B. Debbaut and M.J. Crochet, *J. Non-Newtonian Fluid Mech.*, 30 (1988) 169–184.
- 7 B. Debbaut, *J. Non-Newtonian Fluid Mech.*, 37 (1990) 281–296.
- 8 R.G. Larson, *Constitutive Equations for Polymer Melts and Solutions.*, Butterworths series in Chemical Engineering, Boston, 1988.
- 9 N. Phan-Thien and R.I. Tanner, A new constitutive equation derived from network theory, *J. Non-Newtonian Fluid Mech.*, 2 (1977) 353–365.
- 10 P. Saramito, Numerical simulation of viscoelastic fluid flows using incompressible finite element method and a θ -method. *Mathematical Modelling and Numerical Analysis*, 28 (1994) 1–35.
- 11 P. Saramito, Simulation numérique d'écoulements de fluides viscoélastiques par éléments finis incompressibles at une méthode de directions alternées; applications, thèse de l'Institut National Polytechnique de Grenoble, 1990.
- 12 R. Glowinski and J. Périaux, Numerical methods for nonlinear problems in fluid dynamics. In: *Proceeding of the International Seminar on Scientific Super-Computer*, Feb. 1987.
- 13 R. Glowinski and P. Le Tallec, *Augmented Lagrangian and Operator Splitting Method in Non-linear Mechanics*, SIAM Studies in Applied Mathematics, 1989.
- 14 P. Saramito, Efficient simulation of nonlinear viscoelastic fluid flows. *J. Non-Newtonian Fluid Mech.*, (1993) submitted.
- 15 P. Saramito, Operator splitting for viscoelastic fluid with a differential constitutive law. *C. R. Acad. Sci. Paris*, (1994) submitted.
- 16 M.J. Crochet and J.M. Marchal, A new mixed finite element for calculating viscoelastic fluid flows. *J. Non-Newtonian Fluid Mech.*, 26 (1987) 77–114.
- 17 A. Fortin and A. Zine, An improved GMRES method for solving viscoelastic fluid flow problems, *J. Non-Newtonian Fluid Mech.*, 42 (1992) 1–18.
- 18 V. Girault and P.A. Raviart, *Finite Element Methods for Navier–Stokes Equations—Theory and Algorithms*, Springer-Verlag, 1986.
- 19 P. Lesaint and P.A. Raviart, *On Finite Element Methods for Solving the Neutron Transport Equation*, Academic Press, Carl de Boor edition, 1974.
- 20 K. Baba and M. Tabata, On a conservative upwind finite element scheme for convection diffusion equations. *RAIRO Numer. Anal.*, 15 (1981) 3–25.
- 21 A.N. Brooks and T.R.J. Hughes, Streamline-Upwind/Petrov–Galerkin formulation for convection dominated flow with particular emphasis on the incompressible Navier–Stokes equations. *Comp. Meth. Appl. Mech. Eng.*, 32 (1982) 199–259.
- 22 J. B. Goodman and R.L. Leveque, A geometric approach to high resolution TVD schemes, *SIAM J. Numer. Anal.* 25 (1988) 268–284.

- 23 B. Debaut, J.M. Marchal, and M.J. Crochet, Numerical simulation of highly viscoelastic flows through an abrupt contraction, *J. Non-Newtonian Fluid Mech.*, 29 (1988) 119–146.
- 24 D.V. Boger, Viscoelastic flows through contractions. *Ann. Rev. Fluid Mech.*, 19 (1987) 57–182.
- 25 R.E. Evans and K. Walters. Flow characteristics associated with abrupt change in geometry in the case of highly elastic liquids, *J. Non-Newtonian Fluid Mech.*, 20 (1986) 11–29.
- 26 U. Cartalos and J.M. Piau, Creeping flow regimes of low concentration polymer solutions in thick solvents through an orifice die. *J. Non-Newtonian Fluid Mech.*, 45 (1992) 231–285.
- 27 U. Cartalos and J.M. Piau, Pressure drop scaling law and structural stress contributions for complex flow of flexible polymer solutions in thick solvents. *J. Non-Newtonian Fluid Mech.*, 44: (1992) 55–93.
- 28 P.J. Coates, R.C. Armstrong, and R.A. Brown, Calculation of steady-state viscoelastic flow through axisymmetric contractions with the EEME formulation, *J. Non-Newtonian Fluid Mech.*, 42: (1992) 141–188.